IEEE Access
Multidisciplinary ⋮ Rapid Review ⋮ Open Access Journal

Received 16 April 2024, accepted 9 May 2024, date of publication 17 May 2024, date of current version 28 May 2024.

Digital Object Identifier 10.1109/ACCESS.2024.3402218

RESEARCH ARTICLE

Propeller-Type Wall-Climbing Robot for Visual and Hammering Inspection of Concrete Surfaces

YUKI NISHIMURA[1], HIROMI MOCHIYAMA[2], (Member, IEEE), AND TOMOYUKI YAMAGUCHI[2]

[1]Research Center for Intelligent Robotics, Zhejiang Laboratory, Hangzhou, Zhejiang 311121, China
[2]Faculty of Engineering, Information and Systems, University of Tsukuba, Tsukuba, Ibaraki 305-8577, Japan

Corresponding author: Tomoyuki Yamaguchi (yamaguchi@iit.tsukuba.ac.jp)

This work was supported by the Japan Society for the Promotion of Science (JSPS) KAKENHI under Grant JP23H01643 and Grant JP20H02106.

ABSTRACT Periodic inspections are necessary in maintaining concrete infrastructures. As efficient and low-cost inspection methods, visual inspection robots and hammering inspection robots to detect cracks and internal defects have been developed, respectively. However, these robots can perform only a single task. To realize multiple tasks by a robot, multiple measurement sensors must be installed considering the stability of the robot on the wall and measurement performance. Parameters, such as weight and size, must be considered to ensure the stability of the robot on the wall. We proposed a propeller-type wall-climbing robot that can capture images and perform hammering simultaneously while moving on the wall. The static model of robot was established by considering various parameters, such as the direction of the propeller's thrust force, weight, and placement of the measurement sensors. This model increases the payload for sensor installation and enables movement on dusty concrete walls with a low friction coefficient. The image captured by the inspection robot was employed for crack detection and width estimation. We confirmed that the hammering sounds generated by the robot showed different frequency characteristics on clear and defective areas. The developed inspection robot can collect adequate data for concrete health monitoring.

INDEX TERMS Climbing robots, inspection robots, robotics and automation in construction.

I. INTRODUCTION

Periodic inspections are necessary to maintain concrete infrastructures. Inspectors must identify cracks on the surface and peeling inside the concrete structures. In Japan, the number of road bridges has reached approximately 700,000, and it is estimated that half the number of bridges will be older than 50 years in 2030 [1]. Therefore, the number of concrete structures and cost of inspection have arisen [2]. Various type of unmanned aerial vehicles (UAVs) and wall-climbing robots have been considered for performing inspections to automate the tasks of detecting cracks and peeling of the structure.

Visual inspection is carried out to find surface defects, such as cracks. UAVs that capture the images of structures were proposed in [3] and [4]. Wall-climbing robots [5], [6], [7], [8], [9] can capture images in places inaccessible to humans. As an efficient and low-cost solution, a wall climbing robot for crack inspection on concrete wall surfaces has been proposed [5], [8]. Although UAVs can perform wide-area imaging, accurately measuring the crack width and length is difficult if the distance between the camera and the wall is unknown during flight. Therefore, additional sensors to measure the distance from the wall and special control methods to maintain this distance during flight are required. Wall-climbing robots are advantageous in measuring the crack width and length because they can be attached to the structure surface and can maintain a constant distance between the camera and the wall.

Hammering and impact inspection robots have been proposed to inspect internal defects [11], [12], [13], [14].

The associate editor coordinating the review of this manuscript and approving it for publication was Hengyong Yu.

© 2024 The Authors. This work is licensed under a Creative Commons Attribution-NonCommercial-NoDerivatives 4.0 License.
For more information, see https://creativecommons.org/licenses/by-nc-nd/4.0/

TABLE 1. Specifications of inspection robots using thrust force.

-	Sekhar et al. [8]	Alkalla et al. [9]	Liang et al [10]	Nishimura et al. [11]	Proposed
Year	2014	2017	2021	2022	2023
Internal inspection	N/A	N/A	N/A	Snap-Hammer	Snap-Hammer
Surface inspection	Camera	N/A	N/A	N/A	Camera
Weight [kg]	0.9	1.7	2.5	1.2	1.97
Maximum thrust [N]	28.42	49	25	23.52	31.36
Propeller attached angle [°]	0	0	0-90	0	20
Minimum friction coefficient []	0.31[c]	0.34[c]	0.23[ab]	0.50[c]	0.30[a](0.23[ad])

[a] calculated by Eq. 2; [b] maximum traction at 60° [10]; [c] calculated by Eq. 3; [d] without inspection tools (m=1.76kg).

A UAV that performs hammering inspection by repeatedly flying and reattaching to the surface to strike the wall has been proposed [12]. UAVs have been equipped with an outer frame to prevent collisions during inspection [13]. Hammering inspection using UAVs requires repeated flight and contact with the wall when striking, which is inefficient. Moreover, the robot may not be able to correctly strike. A suction-type wall-climbing robot with an impact echo system has been developed [14]. The suction-type robot shows high mobility on a smooth surface but cannot easily move on rough concrete surfaces while carrying inspection tools. Our previous study [11] proposed a propeller-type wall-climbing robot for hammering inspection. It achieved locomotion on vertical walls by pushing the robot body against the wall using the thrust force of the propeller [7], [9]. We ensured that the distance between the robot and the wall was constant such that uniform strokes and striking forces were realized.

The robot specifications change depending on the operation, necessitating an effective utility robot technology [15]. However, there does not seem to exist development customized depending on the complexity of different inspection robots [16]. In previous studies, various types of inspection robots have been developed, but most robots are intended for a single task. As summarized in Table 1, a wall-climbing robot capable of performing both surface and internal concrete inspection has not yet been developed. For example, our previous robot [11] can perform hammering inspection; however, this robot could not be used for visual inspection because it could not carry a camera to capture images owing to a limitation of its payload. When adding multiple measurement sensors to accomplish multiple tasks, the sensors must be placed by considering both the stability of the robot on the wall and measurement performance. This complicates the robot design because various parameters, such as weight and size, must be appropriately set to ensure the stability of the robot on the wall during the inspection.

Therefore, we proposed a propeller-type wall-climbing robot capable of both image capturing and hammering inspection. Wall-climbing robots are suitable for these purposes because they can attach to the surface from a fixed distance and maintain a constant force. In this study, a static model was established by considering the direction of the propeller's thrust force, weight, and placement of measurement sensors. This model increases the payload for sensor installation and enables movement on dusty concrete walls with a low friction coefficient.

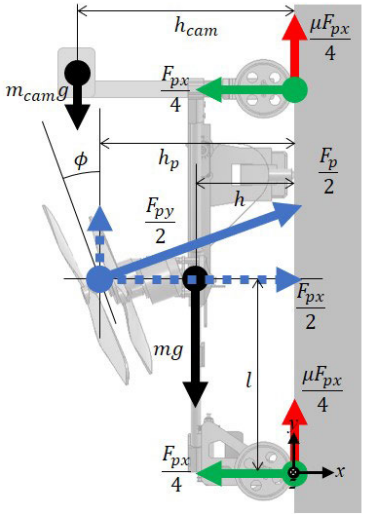

FIGURE 1. Force diagram of the robot in a vertical position.

The key contribution of this study is the development of a highly customizable inspection robot based on the proposed theory to perform multiple inspection functions. We implemented crack imaging and internal defect detection to demonstrate its multi-functionality. The image captured by the inspection robot was utilized for crack detection and width estimation. In addition, we confirmed that the hammering sounds generated by the robot showed different frequency characteristics on clear and internal defect areas. The developed inspection robot is capable of data collection for concrete health monitoring.

The remaining paper is organized as follows. The static model of the robot is proposed in Section II. The design and development of the robot are described in Section III. The experiments on the stability of the robot on the wall, hammering, and image inspection are conducted in Section IV. Section V discusses the experimental results, and Section VI concludes this paper.

II. PROPOSED MODEL OF ROBOT

We proposee a static model of a new wall-climbing robot. The proposed robot is equipped with two propellers at a certain angle ϕ along the vertical surface to increase the payload capacity. Fig. 1 shows the diagram of forces applied to a robot

on a vertical surface in the vertical direction. All forces have a direction. The positive direction of the x-axis is the direction from the ground to the ceiling, and the positive direction of the y-axis is the direction from the robot to the wall. The thrust force F_{px} can be divided into the force to push against the wall and the force to support the robot against gravity. The condition that the robot does not slip on a surface with a friction coefficient μ is

$$\mu F_p \cos\phi + F_p \sin\phi > (m + m_{tool})g \tag{1}$$

where the gravitational acceleration is g, the mass of the robot is m, and the mass of the inspection equipment (e.g., camera) is m_{tool}. From Eq. 1, the minimum friction coefficient at which the robot does not slip is given by

$$\mu_{min} = \frac{(m + m_{tool})g - F_p \sin\phi}{F_p \cos\phi}. \tag{2}$$

Further, the minimum friction coefficient for a robot with no propeller angle (i.e., $\phi = 0°$) is expressed as

$$\mu_{min} = \frac{(m + m_{tool})g}{F_p}. \tag{3}$$

The propeller angle prevents the robot from flipping over on the surface. Moreover, the moment of the inspection tools carried by the robot affects the stability of the robot on the wall. Therefore, considering the moment along the direction of the robot's flipping which includes the propeller tilt angle is necessary. When h_{tool} is the distance from the surface to the camera, h is the distance from the surface to the robot center, and l is the distance from the rear wheel to the robot center. The center of the moment is the contact point of the wall and the wheel which is the one positioned at the very bottom on the wall among four wheels. The direction of the moment is defined since the clockwise is positive. $N_{up-right}$ is the normal force applied to the upper-right wheel and $N_{up-left}$ is the normal force on the upper-left wheel. The moment with the tilt angle of the propellers is

$$\begin{aligned} M = &-h_{tool} m_{tool} g + h_p F_p \sin\phi \\ &+ lF_p \cos\phi - hmg \\ &- 2\,lN_{up-left} - 2\,lN_{up-right} \end{aligned} \tag{4}$$

where h_p is the distance from the surface to the propellers. The moment applied to the robot satisfies $M = 0$ when the robot does not flip over from the wall. Assuming that the robot is in a vertical direction on the wall ($\psi = 0°$), the normal forces on the right and left sides are equally distributed. Therefore, $N_{up-left}$ and $N_{up-right}$ is calculated using Eq. 4 when $M = 0$.

$$\begin{aligned} N_{up-left} &= N_{up-right} \\ &= \frac{-h_{tool} m_{tool} g + h_p F_p \sin\phi + lF_p \cos\phi - hmg}{4l}. \end{aligned} \tag{5}$$

When $N_{up-left}$ and $N_{up-right}$ are larger than 0 N, the robot pushes its body against the wall to avoid flipping over.

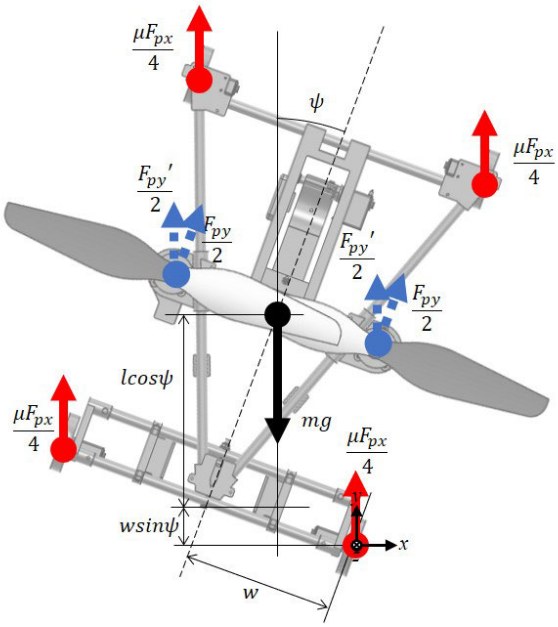

FIGURE 2. Force diagram of the robot at the position with an angle of ψ from the vertical line.

The parameters such as h_p and l should be properly chosen to maintain a stable attitude.

When the robot interacts with the surface with a force F_{impact} at l_{impact}, Eqs. 1 and 4 are rewritten as

$$\begin{aligned} &\mu(F_p \cos\phi - F_{impact}) \\ &\qquad + F_p \sin\phi > (m + m_{tool})g \end{aligned} \tag{6}$$

$$\begin{aligned} M = &-h_{tool} m_{tool} g + h_p F_p \sin\phi \\ &+ lF_p \cos\phi - hmg - l_{impact} F_{impact} \\ &- 2\,lN_{up-left} - 2\,lN_{up-right}. \end{aligned} \tag{7}$$

During hammering inspection, the hammering force has a strong impulse but occurs for a short time. In our previous study [11], the peak hammering force was measured at 215.9 N but the average value in unit time during a hammering sequence was 2.48 N. Therefore, it had limited influence on the stability of the robot on the wall.

The propeller angle can help the robot to climb up on the surface with a small friction coefficient. However, because of the propeller angle, the stability of the robot on the wall is affected when the robot changes its direction. Fig. 2 illustrates the force diagram when the robot turns right with angle ψ. The component of the thrust force in the x direction in Fig. 1 is not affected by the direction change because it is lateral to the surface. Therefore, the sum of the friction forces applied to each wheel does not change. However, the component of the thrust force in the y direction in Fig. 1 is divided into two forces along the y and z axes. Hence, the stable condition in Fig. 2 is applied to avoid slipping when the robot changes direction with angle ψ from the vertical line, and the moment

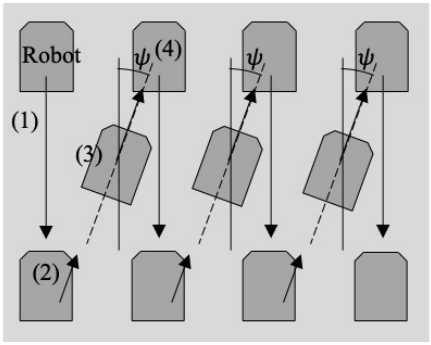

FIGURE 3. Sawtooth-shaped path. (1) Robot descends to the edge of the wall; (2) climbs up while slightly changing direction within ψ; (3) recovers its position in the vertical direction at the top edge of the wall; and (4) descends again to repeat (1) to (4).

applied to the robot to avoid flipping are expressed as

$$\mu F_p \cos\phi + F_p \sin\phi \cos\psi > (m + m_{tool})g \tag{8}$$

$$\begin{aligned} M = &-h_{tool} m_{tool} g + h_p F_p \sin\phi \cos\psi \\ &+ (l \cos\psi + w \sin\psi) F_p \cos\phi - hmg \\ &- (2l + w \sin\psi) N_{up-left} \\ &- (2l - w \sin\psi) N_{up-right} \\ &- (2w \sin\psi) N_{bottom-left} \end{aligned} \tag{9}$$

where w is half the robot width. The maximum change in direction that the robot can make without slipping, ψ_{max}, can be calculated using Eq. 8. When $\psi_{max} < 90°$, the robot cannot turn at right angles.

However, the robot still needs to cover the surface for inspection. The proposed robot has a limitation on the steering action, the sawtooth-shaped path was selected (Fig. 3). The sawtooth-shaped path can minimize the steering actions of the robot by taking advantage of its backward motion [17]. First, the robot moves to the bottom of an area and then changes direction within ψ_{max}. The robot climbs up diagonally and changes the direction vertically after reaching the top. By repeating this sequence, the robot can cover the target area.

III. ROBOT DEVELOPMENT

We developed the inspection robot based on the model presented in Section II to realize a multi-functional inspection robot for surface and internal inspection of a concrete structure. In this section, we (A) validated the robot's stable condition with different propeller installation angles when installing the sensors, (B) presented the specifications of the developed robot, and described (C) the data analysis method used for surface defect detection and (D) internal defect detection.

A. ROBOT DESIGN BASED ON MODEL

The friction coefficient was measured in advance to design the propeller installation angle of the robot. The friction coefficient was 0.36 on a dusty concrete surface and 0.72 on a normal test concrete surface. Based on the specifications of

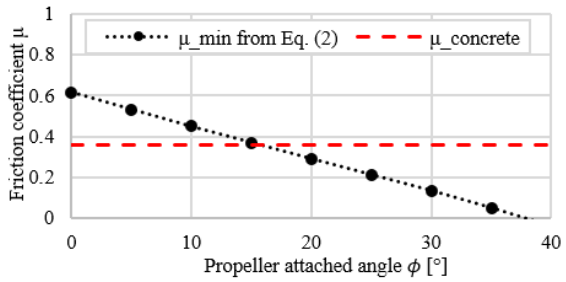

FIGURE 4. Propeller angle vs. minimum friction coefficient. The robot can maintain a stable attitude on a dusty concrete surface when ϕ is over 20°.

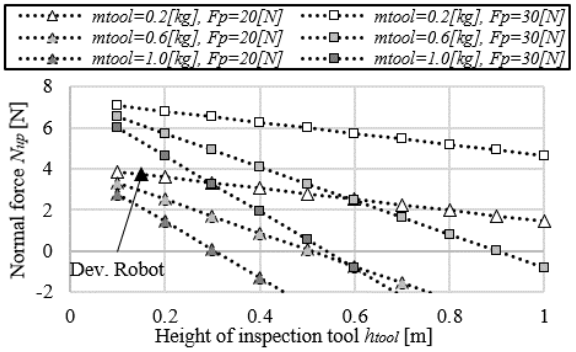

FIGURE 5. Height of tool vs. normal force of upper wheel from Eq. 5 (μ=0.72, ϕ=20°). When N_{up} is negative, the robot flips over.

the parts, we assumed the total mass of the robot to be 1.85 kg. h, h_p, and l in Fig. 1 are 0.09, 0.18, and 0.18 m, respectively. We installed a camera with mass m_{tool} of 0.15 kg for crack inspection. mg is 19.6 N when g is 9.8 m/s^2. The robot must withstand this value to avoid slipping. The maximum thrust force F_p is 31.36 N. When $\phi = 0°$, the minimum friction coefficient at which the robot does not slip, μ_{min}, is calculated as 0.63 from Eq. 3. Therefore, the robot with no propeller angle cannot maintain a stable attitude on a dusty concrete surface.

The propeller installation angle must be set such that the robot can keep a stable attitude even on a concrete surface under dusty conditions. Fig. 4 shows the relationship between the propeller angle and the minimum friction coefficient to avoid slipping from the wall. We calculated changes of μ_{min} when ϕ is increased from 0° to 40° with 5° increments shown as a dashed line in Fig. 4. As a reference, μ on dusty concrete is shown in a red dashed line. The robot will not slip down from the surface when the coefficient of the actual surface is larger than this minimum value ($\mu > \mu_{min}$). When ϕ is over 20°, μ_{min} satisfied this condition even on dusty concrete. Therefore, we set the propeller installation angle of the developed robot is 20°. When ϕ is 20°, the force to push the wall is 29.47 N, and the thrust force along the wall is 10.73 N. Under the dusty concrete condition, the left side of Eq. 1 is 21.34 N. Therefore, the thrust force can support mg of 19.6 N.

A camera as an image sensor should be mounted on the robot to facilitate crack inspection. Fig. 5 depicts the variation

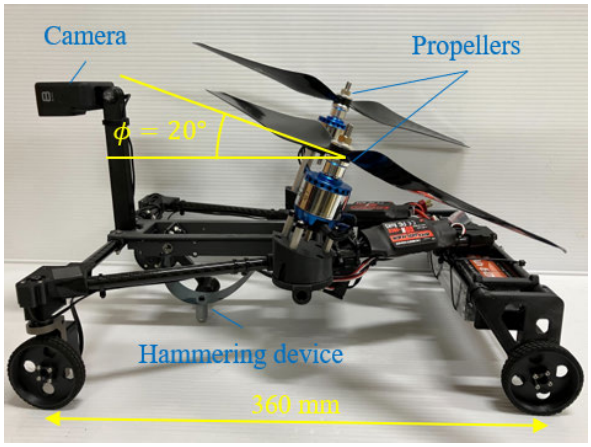

FIGURE 6. Side view of the developed robot.

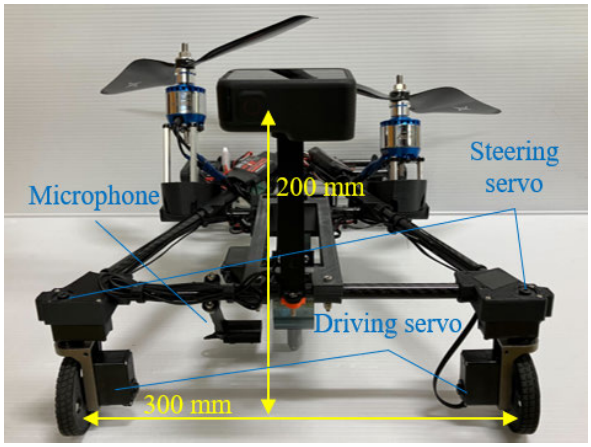

FIGURE 7. Front view of the developed robot.

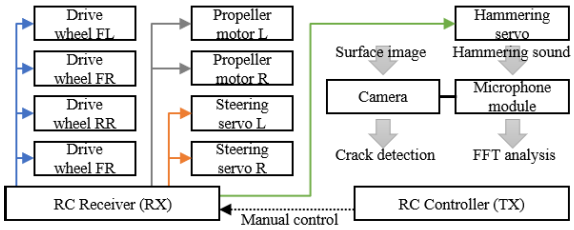

FIGURE 8. Wire diagram of control commands.

in the conditions affecting the stability of the robot on the wall when h_{tool} and m_{tool} change. When m_{tool} is 0.2, 0.6, or 1.0 kg and F_p is 20 or 30 N, N_{up} along the horizontal axis is calculated by increasing h_{tool} from 0.1 to 1.0 m in 0.1-m increments. When N_{up} is less than 0, the wheel cannot push against the wall and becomes unstable. The robot slips when F_p is 20 N and m_{tool} is 0.6 or 1.0 kg. These cases have corresponded to symbols that are bounded by broken lines in Fig. 5. As shown in Fig. 5, although a larger F_p supports the robot, the larger the values of h_{tool} and m_{tool}, the smaller is N_{up}. In this study, GoPro Hero 8 was utilized for the mounted camera as the inspection tool. We estimated the mass of the camera including a frame to be 0.15 kg, and its focal length is 0.2 m from the object. We designed the inspection tool with mass m_{tool} of 0.15 kg, positioned at $h_{tool} = 0.2$ m. With this setting, $N_{up-left}$ and $N_{up-right}$ were 5.17 N when ϕ was 0° and 7.37 N when 20° based on Eq. 5. Although the normal force of the upper wheels is larger than 0 N under both conditions, the proposed method provides a greater margin. From Eq. 8, the robot can change direction within 33° on a normal concrete surface. When capturing the image from this height, the resolution is sufficient for crack detection (see III-C). The result of applying the parameters of this robot is shown by a black triangle in Fig. 5. The condition of the stability of the robot on the wall can be satisfied even when F_p is 20 N.

B. DEVELOPED ROBOT

The developed robot is shown in Figs. 6 and 7. Two propellers were installed at 20° from the vertical surface. These generated the necessary thrust force to stabilize the robot's attitude. The frame of the robot was made of carbon pipes, and other parts were made through 3D printing. The length, width, and height including the propellers were 400, 360, and 280 mm, respectively. The robot used two-wheel steering and four-wheel drive. Continuous-rotation servomotors were used for both steering and driving. The robot mass was 1.76 kg, the camera with its mount was 0.14 kg, and the hammering device was 0.07 kg. The total weight was 1.97 kg. The maximum specified thrust was 31.36 N, and its duration was approximately 9 min for the maximum thrust output. The highest speed was 13.3 m/min. The robot was manually controlled using an RC controller, as shown in Fig. 8. The developed system realized data collection (both images and sounds) online and real-time, and the analysis of the collected data by the robot was done offline after the robot operation.

C. SURFACE INSPECTION

The mounted camera (GoPro Hero 8) could capture 4K (3840×2160) images at a distance of 0.2 m from the surface. The constant distance between the camera and the wall simplified the estimation of the crack lengths and widths. The original images contained the robot's frame and wheels. Hence, the images were cropped to contain only the wall surface. Fig. 9 shows the robot-captured image of a crack scale fixed on the wall. We confirmed that a crack width of 0.04 mm could be visible in images under the illuminance of the concrete wall of 30–50 lx. The relationship between the length and pixels was determined. The crack scale length of 80 mm in the captured image has a resolution of 787 px.

A semantic segmentation model was implemented for pixel-base crack prediction [18]. We trained the model with the crack image and annotation dataset provided in [19]. U-Net [20] and feature pyramid network (FPN) [21] were used for the network architecture. The learning settings for the U-Net and FPN models were an image size of 320 × 320, a learning rate of 0.0001, and a batch size of 1. The encoder was resnext50_32 × 4d and a metric was intersection over

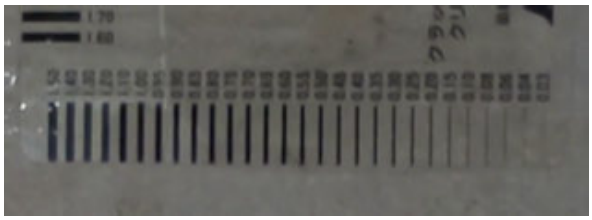

FIGURE 9. Captured image of a crack scale containing black lines with a width of 0.03–1.50 mm.

union (IoU). The resulting IoU of U-Net was 0.9564 and that of FPN was 0.9575 for training validation after 40 epochs. Because the FPN showed slightly higher IoU than U-Net, it was used in the subsequent experiment.

In the crack detection process, the wall surface image captured by the robot was applied with a filter to remove blurring and sharpen the edge. Then, the image was applied to the FPN model for crack detection. Fig. 10 illustrates the crack detection result. Subsequently, the noise was removed from the prediction result. Based on [22], the crack width calculation can be performed when applying Hilditch thinning to the binarized image in the crack detection result [23]. In this method, every pixel in the final thinned lines has information on how many pixels were eliminated during the thinning. In [22], the number of eliminated pixels was utilized as the crack width. The maximum crack width is important for the assessment of concrete health. Thus, the maximum width was calculated from the pixels of the thinned lines.

D. HAMMERING INSPECTION

Hammering inspection determines the internal defects based on changes in the sound generated by the hammering. Because the robot has limited payload capacity, a light hammering device capable of generating a sufficient strike is needed. Therefore, an actuator carrying a steel strip was proposed in [24]. This study employed a steel strip with a length of 200 mm, a width of 30 mm, and a thickness of 0.15 mm as the hammering device, which is adopted in [11]. In propeller-type robots, the propeller noise drowns out the hammering sound. A frame with a microphone cover was prepared to reduce noises and record the hammering sounds close to the hammering position. Fig. 11 shows a hammering sequence of the developed device. In the initial position, the steel strip was bent by the servomotor. When the striking sequence began, the servomotor rotated to stretch the steel strip. When the servomotor angle exceeded a certain value, the steel strip stretched at once and the hammerhead hit the wall. The UAV-type striking system has an 88% hammering success rate [12] but the wall-climbing robot achieved 100% success because it could stably stick to the wall during hammering.

IV. EXPERIMENTS

Both surface and internal inspection experiments were performed on the test concrete structure shown in Fig. 12

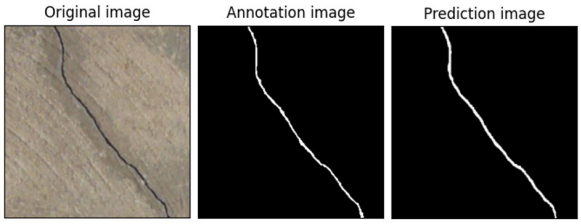

FIGURE 10. Prediction result. Crack and annotation images are from [19].

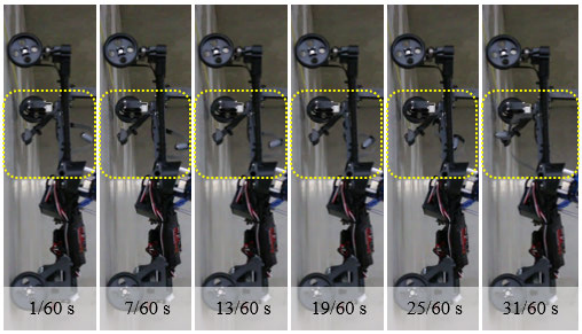

FIGURE 11. Hammering sequence by the robot on a wall. The hammering sequence was filmed at 60 fps, and the figure shows the hitting motion.

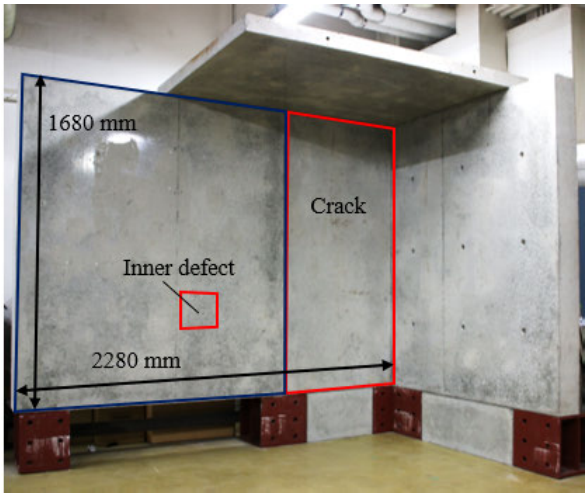

FIGURE 12. Test concrete structure.

using the developed robot. The test concrete structure had an internal defect as the plastic plate inside the concrete on the left side of the wall. An artificial crack existed on the right side of the test structure.

A. CLIMBING EXPERIMENT

A climbing experiment was conducted to verify the climbing ability of the developed robot. Inspection robots need to cover target areas without omission. However, the proposed robot cannot make turns over 33° due to the propeller installation angle in Eq. 8. Therefore, the steering angle was limited to 33°. The robot should cover the target area without exceeding this angle (see Fig. 3). Fig. 13 shows the robot movement: (1) the robot descends to the edge of the wall;

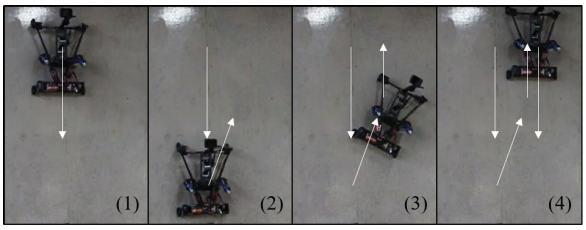

FIGURE 13. Climbing experiment. Numbers correspond to Fig. 3.

(2) the robot climbs up while slightly changing its direction within the constraint on ψ; (3) the robot recovers its position in the vertical direction at the top edge of the wall; (4) the robot descends and repeats (1) to (4). We confirmed that the robot could climb the wall while shifting rightward on the surface.

B. CRACK CAPTURING AND DETECTION EXPERIMENT

First, we verified the image-capturing ability of the robot while moving over a defective area of the test structure. The video resolution was 3840 × 2160 px, the frame rate was 30 fps, and the illuminance of the concrete wall was 30–50 lx.

Figs. 14(a) and 14(c) show that the cropped frames from the captured video included cracks. Figs. 14(b) and 14(d) illustrate the crack detection results discussed in Section III-C. Cracks are displayed in white pixels and the background is in black. The comparison between Figs. 14(a) and 14(b) shows that most of the cracks are detected. However, the crack in the middle lower part of the image could not be detected because it was considerably narrow. Based on Figs. 14(c) and 14(d), the crack at the center of the image was distinct but the thin crack did not appear clearly in the prediction image. Fig. 14(c) is blurred when compared with Fig. 14(a); therefore, the crack detection result was not as accurate as that presented in Fig. 14(b).

In Fig. 14(b), the maximum crack width was 85 px in the image. The crack width was predicted based on the width per pixel measured in advance (0.1 mm/px). The resolution can be constant because of the characteristic of the proposed robot that can always stack to the wall and keep a constant distance between the camera and the wall. Thus, the calculated crack width was 8.5 mm whereas the actual crack width measured by the scale was 8 mm.

The computational time for processing the robot-captured image was 44.73 s in average of ten trials (31.70 s for crack detection and 13.03 s for width calculation. These computational times were obtained from our program on a computer with an Intel i7 processor running at 2.8 GHz using 16 GB of RAM, running Windows 11. As described in Section III-B, all the inspection processes of the data collected by the robot are done offline. The quality of the captured image affects the detection result, but it does not affect the computational time because the proposed robot can capture images at a constant distance from the wall with the constant resolution and image size. Since the images are taken as videos, the same location is included in multiple frames. The overall computational time can be reduced by reducing the number of frames to process even if the time to process a single image remains the same.

C. HAMMERING EXPERIMENT AND SOUND ANALYSIS

Hammering sounds were collected to investigate the frequency difference between clear and defective areas. The hammering sounds were recorded by the microphone module while the robot stabilized its attitude on the wall with its thrust force. Three patterns of hammering sounds under different thrust forces—small (approximately 20 N), medium (approximately 25 N), and large (approximately 30 N)—were collected. In addition, hammering sounds without additional noise were recorded by holding and pushing the robot by hand. Hammering was performed five times at clear and defective points under four conditions (no-noise, small-thrust, medium-thrust, large-thrust). Fourty hammering sounds were collected. The fast Fourier transform (FFT) was applied to the collected sounds in eight patterns. Fig. 15 illustrates the FFT results as the average of 100 Hz bands. The amplitude of the spectrum was normalized by the intensity of the first peak. Thin colored lines in each figure indicate the FFT result in each hammering, and the thick line represents the average of five hammerings. Furthermore, the first ten peaks were calculated and plotted as red dots.

A comparison of Figs. 15(a) and (b) shows that both clear and defect sounds have peaks at 5200 Hz when there is no propeller noise. Defect sounds had additional characteristic peaks at 3000, 3800, and 4600 Hz. Dotted vertical lines at 3000, 3800, 4600, and 5200 Hz show the characteristic peaks of clear and defect sounds. Figs. 15(c) to (h) show the case when the results were affected by propeller noise. When the thrust force was small, the peaks at 3000, 4600, and 5200 Hz were not observed in both results, as shown in Figs. 15(c) and (d). However, the defect sounds showed a peak at 3800 Hz, labeled as the fifth peak in Figs. 15(d). When the thrust force was medium, the peaks at 3000, 4600, and 5200 Hz were not observed but the defect sound showed a peak at 3800 Hz, as shown in Figs. 15(e) and (f). The results for small and medium thrust forces showed similar shapes. Figs. 15(g) and (h) show the result when the thrust force is large. When the thrust force reached the maximum value, the aforementioned frequency peaks did not appear in the result.

From the frequency characteristics identified from the collected data, we confirmed that it was possible to classify the hammering sounds. Ikeda and Kamimura [25] introduced a statistical method for classification. This method used the difference in intensity of a certain frequency between clear and defect sounds. The threshold was determined by adding a quarter of the largest difference in intensity between clear and defect sounds to the smaller value. In this study, we calculated the thresholds by using the difference in the average intensity between the clear and defect sounds at 3800 Hz because the characteristic

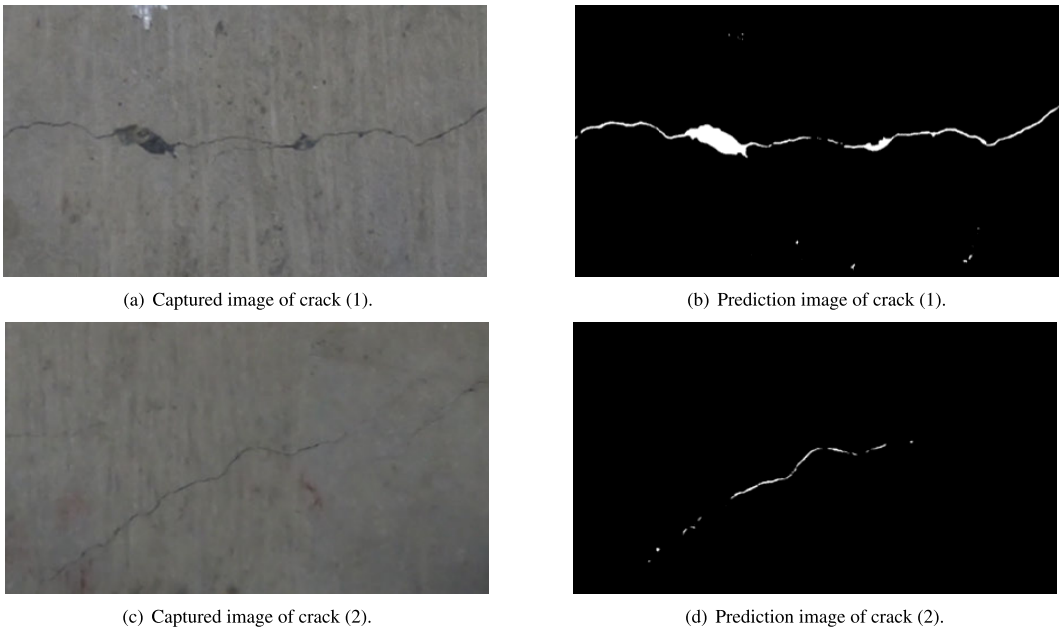

(a) Captured image of crack (1).
(b) Prediction image of crack (1).
(c) Captured image of crack (2).
(d) Prediction image of crack (2).

FIGURE 14. Captured images and prediction results.

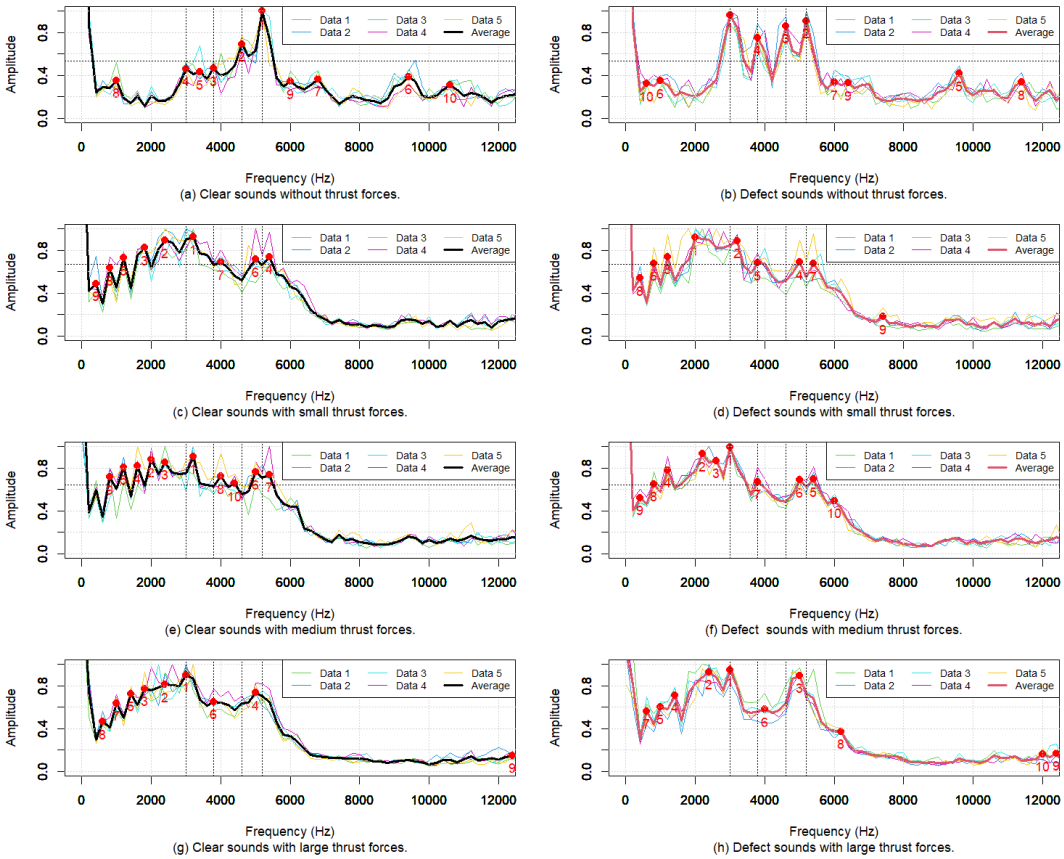

FIGURE 15. FFT results of hammering sounds.

frequency appeared at 3800 Hz in the above analysis. The calculated thresholds under no thrust and small and medium thrust were 0.54, 0.67, and 0.58, respectively (see the horizontal dashed lines in Fig. 15(a) to (f)). The classification results are shown in Table 2. TP, TN, FP, and FN represent the True Positive, True Negative, False Positive,

TABLE 2. Classification results based on the amplitude threshold.

	no-noise	small	medium	total
TP	5	4	3	12
TN	4	3	3	10
FP	1	2	2	5
FN	0	1	2	3
Accuracy	0.9	0.7	0.6	0.73
Perception	0.83	0.67	0.6	0.71
Recall	1	0.8	0.6	0.8
F_1-score	0.9	0.73	0.6	0.75

and False Negative data, respectively. Under a large thrust condition, the peak at 3800 Hz was not observed for both clear and defect sounds; thus, we excluded them from the analysis. Overall, we obtained an accuracy of 73%. The accuracy under the no-noise condition was 90%, which decreased as the thrust strength increased. The accuracy under medium thrust was 60%.

V. DISCUSSION

The proposed robot with inspection tools can maintain its attitude on the surface with the minimum friction coefficient of 0.30. This value is sufficient because the minimum friction coefficient on dusty concrete surface is 0.36. From Table 1, Liang et al.'s robot [10] overcomes the wall friction with a friction coefficient of 0.23. This was because most previous studies did not consider the weight of the inspection tools. The proposed robot could climb with a friction coefficient of 0.23 when it did not carry any inspection tools.

The permissible crack width for reinforced concrete is 0.41 mm for dry air or under protective membrane exposure conditions [26]. Therefore, the robot needs to recognize crack widths of more than 0.41 mm. The captured image from the mounted camera showed a 0.4 mm line of the crack scale to facilitate concrete assessment by the robot. We trained the U-Net and FPN using the crack dataset provided in [19] and applied it to the robot-captured image. In addition, the crack width estimation result showed that the maximum crack width estimated by the program was 8.5 mm, whereas the actual width was 8 mm. The error was +0.5 mm and percentage error was 6%. The pixel and width information can be utilized to calculate the crack width because the developed inspection robot can maintain a constant distance between the wall and camera. The result shows that the image captured by the inspection robot can be used for crack width detection. However, we tested only two types of network architecture and the detection result was not perfect. A deeper analysis is required to identify a suitable crack detection network.

We confirmed that the hammering sounds generated by the developed inspection robot showed different frequency characteristics when hammering at clear and defect areas. The noise increases when the thrust increases. Therefore, FFT was applied for three thrust forces. The clear sound showed a peak at 5200 Hz, whereas the defect sound showed peaks at 3000, 3800, and 4600 Hz. Based on these results, defects can be detected by observing the peaks at 3800 Hz when the thrust is small or medium. With a small thrust force, the robot can climb the test concrete structure without slips. From Eq. 2, the robot with a small thrust output can climb the wall with a coefficient of over 0.67, whereas the robot with a medium thrust output can climb the wall with a coefficient of over 0.46. The actual friction coefficient was 0.72 for the test concrete structure. We classified the hammering sounds based on the average difference in amplitude at 3800 Hz. The robot could inspect the test structure with a friction coefficient of 0.72, achieving an accuracy of 70%. However, the thrust force must be set to a large value when the inspection robot moves on a wall with a low friction coefficient of less than 0.47. Consequently, the hammering inspection accuracy will decrease. Therefore, improvement of strategies for noise reduction is needed.

VI. CONCLUSION

In this study, we described a method for developing a propeller-type wall-climbing robot that has both image capturing and hammering inspection functions. The proposed design uses the propeller thrust direction and placement of the inspection tools as parameters to increase the payload, apply low friction coefficients, and realize a multi-functional robot capable of image and sound sensing. Thus, the robot with $\phi = 20$, $h_{tool} = 0.2$, and $m_{tool} = 0.14$ was developed. Furthermore, we described a software design for both crack image detection and hammering sound measurement.

In the experiments, the inspection robot showed its ability to collect both image and sound data. We realized the crack image capturing by the robot and implemented the neural network-based crack detection and the width estimation, which can convert the width from pixels to mm. Sound data were utilized for internal concrete defect analysis. In our previous study [11], only the hammering sound with a constant propeller noise was analyzed with deep learning. In this study, we analyzed the frequency characteristics of hammering sounds recorded under different strengths of thrust forces.

Future research should focus on building an inspection system to analyze the damage to concrete in a real-time. The crack detection algorithm has a large scope for improvement. Width calculation was realized using a thinning-based method [22], but further improvement of the accuracy and comparison with other methods, such as [27] and [28], are expected. Although the software for the detection method needs improvement, this paper introduced a method to increase the payload capacity of the existing propeller-type wall-climbing robot. We focused on wall climbing and wall inspection, but it will be necessary to also cover inspections of ceilings and curved shapes. Especially when moving on a ceiling, it may be easier to control the robot's position without a propeller angle. Therefore, exploring the possibility of incorporating variable propeller angles by modifying its design is advantageous.

REFERENCES

[1] M. Shirato and T. Tamakoshi, "Bridge inspection standards in Japan and U.S.," in *Proc. 29th U.S.-Japan Bridge Eng. Workshop*, 2013, pp. 129–142. [Online]. Available: https://thesis.pwri.go.jp/files/doken_shiryou_4279_00.pdf
[2] J. Nojima, T. Mizobuchi, and K. Hayashi, "Research and development of infrastructure diagnostic robot system (ALP) for detailed inspection of concrete structures at elevated heights," *J. Adv. Concrete Technol.*, vol. 17, no. 9, pp. 526–541, 2019.
[3] T. Saida, M. Rashid, Y. Nemoto, S. Tsukamoto, T. Asai, and M. Nishio, "CNN-based segmentation frameworks for structural component and earthquake damage determinations using UAV images," *Earthq. Eng. Eng. Vib.*, vol. 22, no. 2, pp. 359–369, Apr. 2023.
[4] Y. Nishimura, M. Sakamoto, and T. Yamaguchi, "Development of multi-copter system on concrete surfaces with outer frame and wind speed sensors," in *Proc. IEEE/SICE Int. Symp. Syst. Integr. (SII)*, Jan. 2020, pp. 909–914.
[5] J.-U. Shin, D. Kim, J.-H. Kim, and H. Myung, "Micro aerial vehicle type wall-climbing robot mechanism," in *Proc. IEEE RO-MAN*, Aug. 2013, pp. 722–725.
[6] L. Yang, B. Li, J. Feng, G. Yang, Y. Chang, B. Jiang, and J. Xiao, "Automated wall-climbing robot for concrete construction inspection," *J. Field Robot.*, vol. 40, no. 1, pp. 110–129, Jan. 2023.
[7] K. Sukvichai, P. Maolanon, and K. Songkrasin, "Design of a double-propellers wall-climbing robot," in *Proc. IEEE Int. Conf. Robot. Biomimetics (ROBIO)*, Dec. 2017, pp. 239–245.
[8] P. Sekhar and R. S. Bhooshan, "Duct fan based wall climbing robot for concrete surface crack inspection," in *Proc. Annu. IEEE India Conf. (INDICON)*, Dec. 2014, pp. 1–6.
[9] M. G. Alkalla, M. A. Fanni, A. M. Mohamed, and S. Hashimoto, "Tele-operated propeller-type climbing robot for inspection of petro-chemical vessels," *Ind. Robot, Int. J.*, vol. 44, no. 2, pp. 166–177, Mar. 2017.
[10] P. Liang, X. Gao, Q. Zhang, R. Gao, M. Li, Y. Xu, and W. Zhu, "Design and stability analysis of a wall-climbing robot using propulsive force of propeller," *Symmetry*, vol. 13, no. 1, p. 37, Dec. 2020.
[11] Y. Nishimura, S. Takahashi, H. Mochiyama, and T. Yamaguchi, "Automated hammering inspection system with multi-copter type mobile robot for concrete structures," *IEEE Robot. Autom. Lett.*, vol. 7, no. 4, pp. 9993–10000, Oct. 2022.
[12] A. Ichikawa, Y. Abe, T. Ikeda, K. Ohara, J. Kishikawa, S. Ashizawa, T. Oomichi, A. Okino, and T. Fukuda, "UAV with manipulator for bridge inspection—Hammering system for mounting to UAV," in *Proc. IEEE/SICE Int. Symp. Syst. Integr. (SII)*, Dec. 2017, pp. 775–780.
[13] C. J. Salaan, K. Tadakuma, Y. Okada, Y. Sakai, K. Ohno, and S. Tadokoro, "Development and experimental validation of aerial vehicle with passive rotating shell on each rotor," *IEEE Robot. Autom. Lett.*, vol. 4, no. 3, pp. 2568–2575, Jul. 2019.
[14] B. Li, K. Ushiroda, L. Yang, Q. Song, and J. Xiao, "Wall-climbing robot for non-destructive evaluation using impact-echo and metric learning SVM," *Int. J. Intell. Robot. Appl.*, vol. 1, no. 3, pp. 255–270, Sep. 2017.
[15] H. Asama and D. Kurabayashi, "Robot technology for super resilience (in Japanese)," *J Soc. Instrum. Control Eng.*, vol. 57, no. 2, pp. 95–100, 2018.
[16] IEEE Transmitter. (Apr. 2023). *How Robots Are Repairing Infrastructure*. [Online]. Available: https://transmitter.ieee.org/how-robots-are-repairing-infrastructure/
[17] A. Papadimitriou, G. Andrikopoulos, and G. Nikolakopoulos, "On path following evaluation for a tethered climbing robot," in *Proc. IECON 46th Annu. Conf. IEEE Ind. Electron. Soc.*, Oct. 2020, pp. 656–661.
[18] P. Iakubovskii. (2019). *Segmentation Models*. GitHub repository. [Online]. Available: https://github.com/qubvel/segmentation_models
[19] X. Yang, H. Li, Y. Yu, X. Luo, T. Huang, and X. Yang, "Automatic pixel–level crack detection and measurement using fully convolutional network," *Comput.-Aided Civil Infrastruct. Eng.*, vol. 33, no. 12, pp. 1090–1109, Dec. 2018.
[20] O. Ronneberger, P. Fischer, and T. Brox, "U-Net: Convolutional networks for biomedical image segmentation," in *Medical Image Computing and Computer-Assisted Intervention—MICCAI 2015*, N. Navab, J. Hornegger, W. M. Wells, and A. F. Frangi, Eds. Cham, Switzerland: Springer, 2015, pp. 234–241.
[21] T.-Y. Lin, P. Dollár, R. Girshick, K. He, B. Hariharan, and S. Belongie, "Feature pyramid networks for object detection," in *Proc. IEEE Conf. Comput. Vis. Pattern Recognit. (CVPR)*, Jul. 2017, pp. 936–944.
[22] T. Yamaguchi and S. Hashimoto, "Practical image measurement of crack width for real concrete structure," *Electron. Commun. Jpn.*, vol. 92, no. 10, pp. 1–12, Oct. 2009.
[23] C. J. Hilditch, "Linear skeletons from square cupboards," *Mach. Intell.*, vol. 6, pp. 403–420, Jan. 1969.
[24] H. Mochiyama, "Model validation of discretized spatial closed elastica," in *Proc. IEEE/RSJ Int. Conf. Intell. Robots Syst. (IROS)*, Oct. 2016, pp. 5216–5223.
[25] K. Ikeda and A. Kamimura, "Hammering acoustic analysis using machine learning techniques for piping inspection," *J. Robot. Mechatronics*, vol. 32, no. 4, pp. 789–797, Aug. 2020.
[26] M. Sahmaran, M. Li, and V. C. Li, "Transport properties of engineered cementitious composites under chloride exposure," *ACI Mater. J.*, vol. 104, pp. 604–611, Jan. 2007.
[27] C. Feng, H. Zhang, H. Wang, S. Wang, and Y. Li, "Automatic pixel-level crack detection on dam surface using deep convolutional network," *Sensors*, vol. 20, no. 7, p. 2069, Apr. 2020.
[28] X. Weng, Y. Huang, and W. Wang, "Segment-based pavement crack quantification," *Autom. Construct.*, vol. 105, Sep. 2019, Art. no. 102819.

YUKI NISHIMURA received the Ph.D. degree in human informatics from the Doctoral Program in Empowerment Informatics, University of Tsukuba, Japan, in 2023. He is currently a Postdoctoral Fellow with the Research Center for Intelligent Robotics, Zhejiang Laboratory, China. His research interests include climbing robots, robotics and automation in agriculture and forestry, robotics and automation in construction, computer vision for automation, telerobotics, and teleoperations.

HIROMI MOCHIYAMA (Member, IEEE) received the B.E. and M.E. degrees in electrical engineering from Waseda University, Tokyo, Japan, in 1993 and 1995, respectively, and the Ph.D. degree in information science from Japan Advanced Institute of Science and Technology (JAIST), Hokuriku, Japan, in 1998. After working with JAIST, the National Defense Academy, and Nagoya Institute of Technology, Japan, he joined the University of Tsukuba, in 2007, as an Associate Professor. Since then, he has directed the Flexible Robotics Laboratory. He is currently a Professor with the Department of Intelligent Interaction Technology, University of Tsukuba, Japan. His research interests include system and control theory for soft robotics and haptics. He served as the Vice President of Financial Activities of IEEE Robotics and Automation Society, from 2022 to 2023. He also served as the Deputy Director of Bureau of Science, Technology and Innovation Policy, Cabinet Office, Japan, from 2010 to 2011.

TOMOYUKI YAMAGUCHI received the Ph.D. degree from Waseda University, Japan, in 2008. In 2013, he joined the University of Tsukuba, where he is currently an Associate Professor with the Department of Intelligent Interaction Technologies. His research interests include image processing, human interface, and robotics.